J. Fluid Mech. (2004), *vol.* 517, *pp.* 209–228.
DOI: 10.1017/S0022112004000643 Printed in the United Kingdom

Onset of wetting failure in liquid–liquid systems

By DAVID JACQMIN

NASA Glenn Research Center, Cleveland, OH 44135, USA

(Received 4 September 2003 and in revised form 24 June 2004)

Some model problems are considered in order to investigate wetting failure in liquid–liquid systems. Three geometries are considered, two-dimensional two-phase shear flow, two-dimensional driven capillary rise, and both two- and three-dimensional two-phase driven cavity flow. In the first two cases, the two fluids are made equiviscous. The driven cavity flow is investigated for both equi- and non-equiviscous fluids. Three methods of analysis are used for the equiviscous case, an essentially exact Fourier series method, a quasi-parallel approximation and a phase-field model. The Fourier series validates the phase-field method in that they both give nearly identical results for onset of instability. At relatively large slip length divided by channel width (10^{-2}), the capillary number at which onset of wetting failure (entrainment of the receding fluid in the advancing) occurs is highly dependent on the type of flow. This dependence, however, appears to diminish rapidly as the slip length becomes smaller. The capillary number for the onset of instability is moderately dependent on gravity level.

Three-dimensional phase-field calculations are then discussed that show wetting failure through tipstreaming and splitting instabilities. Spot checks indicate that the onset points of two- and three-dimensional instabilities are very close. It is hypothesized that tipstreaming can be understood in part as a quasi-two-dimensional phenomenon.

1. Introduction

In successful dynamic wetting of a solid, the advancing fluid completely displaces the receding. When the liquid advances at too high a speed, however, some of the receding fluid is engulfed as a film or as droplets or bubbles. Understanding of what determines the transition to wetting failure is still very limited. Still unknown are the relative importance of nanoscale, mesoscale and macroscale (experiment or process scale) effects.

This paper applies three different approaches to calculating wetting failure in liquid–liquid systems: quasi-parallel analysis; diffuse-interface numerical simulations using a phase-field model of capillarity; and numerical solutions using Fourier series solutions of the full Stokes equations with sharp interfaces. The goal of this work is to be able to calculate three-dimensional tipstreaming instabilities at wetting lines. The phase-field approach shows promise for this because it has diffusive mechanisms to deal with and resolve the wetting and interface-tearing near-singularities that occur in wetting tipstreaming flows and because it can deal with complicated and multiple interfaces. However, it can be a difficult and sometimes expensive method. The tipstreaming problem is therefore approached through some easier two-dimensional wetting problems for which the quasi-parallel and Fourier series methods are applicable and results from the three methods can be compared. In this way, we

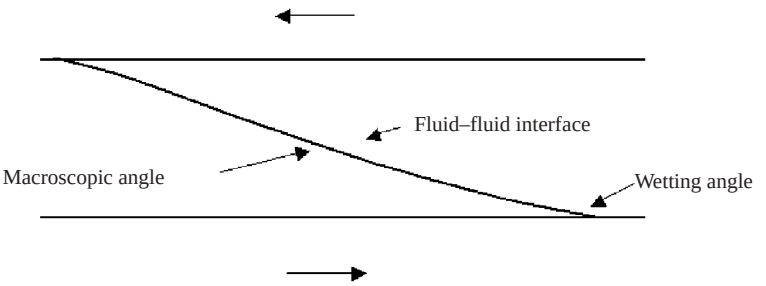

FIGURE 1. Interface for the shear-flow equiviscosity case with oppositely moving walls and opposite wettabilities. The interface is antisymmetric about $x = 0$, where x is the horizontal coordinate. Gravity points to the right toward the denser fluid.

attempt to build confidence in the phase-field method, which is then briefly applied to the full problem of three-dimensional tipstreaming.

Kistler (1993) gives perhaps the best review of wetting failure. The usual assumption is that failure occurs as the dynamic wetting angle approaches 180°. This has been frequently observed for liquid–air systems, but, as will be shown, does not hold for liquid–liquid wetting. Near the threshold of wetting instability, the contact line often becomes corrugated and then V-shaped (Blake & Ruschak 1979; Burley & Jolly 1984; Ghannam & Esmail 1993). Blake & Ruschak have hypothesized that these V shapes form because they effectively reduce the speed of wetting (the velocity component normal to the wetting line is reduced). Experiments by Simpkins & Kuck (2000, 2003) have shown that the Vs can elongate and become subject to tipstreaming. There seem to be no previous computations of tipstreaming during wetting. Calculations have been made for tipstreaming from cusps on bubbles in extensional flow (Siegel 2000; Eggers 2001; Eggleton, Tsai & Stebe 2001).

For both two and three dimensions, wetting failure can be investigated in what are essentially two-phase driven cavities with Stokes flow (Somalinga & Bose 2000). We consider three particular cases. In the first, shown in figure 1, both walls move at the same speed in opposite directions – a Couette-like flow. This case is symmetrized, for reasons given below, by the walls having opposite wettability. The second case has the walls moving in the same direction. This case is given the constraint of no net flow of fluid (endwalls at $\pm\infty$). The resulting flow is like a pressure-driven capillary-rise or slug flow, with the rise speed equalling the negative of the speed of the walls. The third case has one wall moving and the other fixed, again with the constraint of there being no net flow of fluid. This is like the classic driven cavity flow. The wetting angle at the unmoving wall is taken to be 90°. This is the case investigated by the three-dimensional calculations. Gravitational forcing can be included in all these flows.

The Couette flow case would be the most difficult to carry out experimentally, but its symmetry gives some advantages in illustrating and discussing basic concepts. It is the only case that allows the application of quasi-parallel modelling, which is useful for making calculations that can resolve very small slip lengths (often nanometer scale). The particular set of conditions that allows the application of quasi-parallel modelling is when the two plates have opposite wettability. In this case, if the equilibium contact angles are high, solutions exist in which the interface is everywhere approximately parallel to the moving plates. Another advantage of the Couette flow case is that it gives a well-defined macroscopic dynamic wetting angle

which, since the interface between the two contact lines is nearly straight, is simply the midchannel angle of the interface or the average angle of the interface from wetting line to wetting line. In other geometries, the macroscopic or dynamic wetting angle can be harder to define. For example, in capillary rise or in droplet spreading the macroscopic dynamic wetting angle sometimes has to be determined indirectly from the macroscopic interfacial curvature (Hocking 1982).

We start by discussing the various analytical and numerical methods. Two-dimensional results are then given. Flow fields are shown, but the main emphasis is on determining the onset of instability (entrainment) as characterized by either a critical capillary number ($\mu U_{cr}/\sigma$, where μ is viscosity, σ is surface tension and U_{cr} is the critical velocity at which entrainment first occurs) or critical macroscopic dynamic angle. Stability limits are found as a function of inner/outer length scale ratio (slip length divided by channel width) and, to a limited extent, gravity level. Both when stable and unstable, the interface can be characterized in terms of a time-dependent macroscopic wetting angle. When stable, the flow evolves toward a steady macroscopic angle. When unstable, the macroscopic angle evolves to 180°. However, the maximum stable macroscopic angle is generally, as will be documented for the Couette-flow case, well short of 180°.

We then present three-dimensional tipstreaming results. The geometry used for these calculations is case 3, the driven cavity. To generate three-dimensional tipstreaming, it is necessary for the fluids to have significantly different viscosities (Grace 1982). The three-dimensional calculations demonstrate three-dimensional tipstreaming at a viscosity ratio of 10 to 1. Some of these calculations are initiated as nearly two-dimensional and show the evolution of small three-dimensional disturbances to tipstreaming. Some three-dimensional critical capillary numbers are calculated, and they are found to be extremely close to those found for two-dimensional instability.

2. Model two-dimensional equations

The two-dimensional model flow for case 1 is shown in figure 1. Cases 2 and 3 are topologically similar. Flow geometries for these cases are indicated in figures 13 and 15. The bottom and top plates are at $y=0$ and H. The interface separating them is at $x=h(y)$. The fluid densities differ by ρ_δ. The gravity vector $\boldsymbol{g}$ points from left to right, towards the denser fluid.

2.1. *The quasi-parallel equations*

These equations are applied only to case 1, for which the fluids are equiviscous with viscosity μ, and the plate speeds are $+U_0$ (bottom) and $-U_0$ (top). The two plates have opposite wettability so that when the fluid is motionless the interface is a straight line angling from plate to plate. The flow that arises from these conditions produces an antisymmetric interface. The centrepoint of the interface lies at $x=0$.

In the leftwards fluid, the quasi-parallel momentum equation is

$$\mu\frac{\partial^2 u_{\mathrm{l}}}{\partial y^2}=\frac{\partial p_{\mathrm{l}}}{\partial x}+\tfrac{1}{2}\rho_\delta g. \tag{2.1a}$$

In the rightwards it is

$$\mu\frac{\partial^2 u_{\mathrm{r}}}{\partial y^2}=\frac{\partial p_{\mathrm{r}}}{\partial x}-\tfrac{1}{2}\rho_\delta g, \tag{2.1b}$$

p is the pressure, u the horizontal velocity. The horizontal velocity boundary condition at the lower plate is

$$u - U_0 = \epsilon_s \frac{\partial u}{\partial y}, \tag{2.2}$$

where ϵ_s is the slip length. The interfacial velocity and tangential stress boundary conditions are

$$u_\mathrm{l}(h) = u_\mathrm{r}(h), \tag{2.3}$$

$$\left.\frac{\partial u_\mathrm{l}}{\partial y}\right|_h = \left.\frac{\partial u_\mathrm{r}}{\partial y}\right|_h, \tag{2.4}$$

and the upper plate horizontal velocity boundary condition is

$$u + U_0 = -\epsilon_s \frac{\partial u}{\partial y}. \tag{2.5}$$

There are two conservation conditions. The y-integrated horizontal flux of each liquid must be zero.

The interfacial normal stress condition is

$$\sigma\kappa = p_\mathrm{r} - p_\mathrm{l}, \tag{2.6}$$

where σ is the surface tension and κ the curvature. This can be differentiated in order to find the x-variation of the interface shape:

$$\sigma \frac{\mathrm{d}\kappa}{\mathrm{d}x} = \frac{\mathrm{d}p_\mathrm{r}}{\mathrm{d}x} - \frac{\mathrm{d}p_\mathrm{l}}{\mathrm{d}x}. \tag{2.7a}$$

Define the interface arclength coordinate s so that it increases with decreasing y (increases as one moves along the interface from channel top to bottom). Noting that x and the interface arclength s are then asymptotically equivalent as the interface angle approaches 180°, instead of (2.7a) we use

$$\sigma \frac{\mathrm{d}\kappa}{\mathrm{d}s} = \frac{\mathrm{d}p_\mathrm{r}}{\mathrm{d}x} - \frac{\mathrm{d}p_\mathrm{l}}{\mathrm{d}x}. \tag{2.7b}$$

The *ad hoc* substitution of s for x on the left-hand side of (2.7b) turns out to allow the application of the quasi-parallel model to wetting angles less than 90°.† Changes in interface angle are calculated from

$$\frac{\mathrm{d}\theta}{\mathrm{d}s} = \kappa, \tag{2.8}$$

where θ is the angle and where again s is used. The interface position is found from

$$\frac{\mathrm{d}y}{\mathrm{d}s} = -\sin(\theta), \quad \frac{\mathrm{d}x}{\mathrm{d}s} = -\cos(\theta). \tag{2.9}$$

† Results from (2.7a) and (2.7b) are in good agreement down to a wetting angle of about 150°. They then diverge, but remain qualitatively similar to about 120°. As the wetting angle approaches 90°, results from (2.7a) fail; for example, the critical capillary number calculated using it goes to infinity. Results from (2.7b) appear to remain useful even to wetting angles of 30°. Why this is so is unclear. The portion of the interface that is at an angle less than 90° is fairly small. It may be that once the interface angle is past 90° the pressure difference across the interface is dominated by a relatively large pressure in the fluid next to the wall and that this pressure is adequately, even though very crudely, captured by the lubrication equations.

The solutions to the momentum equations are

$$u_{\rm l} = \frac{1}{\mu}\left(A_{\rm l} + B_{\rm l} y + \tfrac{1}{2} p_{{\rm l},x} y^2 + \tfrac{1}{4}\rho_\delta g y^2\right), \tag{2.10a}$$

$$u_{\rm r} = \frac{1}{\mu}\left(A_{\rm r} + B_{\rm r} y + \tfrac{1}{2} p_{{\rm r},x} y^2 - \tfrac{1}{4}\rho_\delta g y^2\right). \tag{2.10b}$$

with $A_{\rm l}$, $B_{\rm l}$, $p_{{\rm l},x}$, $A_{\rm r}$, $B_{\rm r}$ and $p_{{\rm r},x}$ found through the system of equations

$$A_{\rm l} - \epsilon_s B_{\rm l} = \mu U_0, \tag{2.11a}$$

$$A_{\rm l} + hB_{\rm l} + \tfrac{1}{2}h^2 p_{{\rm l},x} - A_{\rm r} - hB_{\rm r} - \tfrac{1}{2}h^2 p_{{\rm r},x} = -\tfrac{1}{2}\rho_\delta g h^2, \tag{2.11b}$$

$$B_{\rm l} + h p_{{\rm l},x} - B_{\rm r} - h p_{{\rm r},x} = -\rho_\delta g h, \tag{2.11c}$$

$$A_{\rm r} + (H+\epsilon_s)B_{\rm r} + \left(\tfrac{1}{2}H^2 + \epsilon_s H\right) p_{{\rm r},x} = -\mu U_0 + \tfrac{1}{2}\left(\tfrac{1}{2}H^2 + \epsilon_s H\right)\rho_\delta g, \tag{2.11d}$$

$$hA_{\rm l} + \tfrac{1}{2}h^2 B_{\rm l} + \tfrac{1}{6}h^3 p_{{\rm l},x} = -\tfrac{1}{12}\rho_\delta g h^3, \tag{2.11e}$$

$$(H-h)A_{\rm r} + \tfrac{1}{2}(H^2 - h^2)B_{\rm r} + \tfrac{1}{6}(H^3 - h^3)p_{{\rm r},x} = \tfrac{1}{12}\rho_\delta g (H^3 - h^3). \tag{2.11f}$$

From this $p_{{\rm l},x}$ and $p_{{\rm r},x}$, the x-derivatives of $p_{\rm l}$ and $p_{\rm r}$, are found as functions of h. Equations (2.7*b*), (2.8) and (2.9) can then be used to advance the curvature, interface angle and h as a function of x.

Since the interface is antisymmetric about $x = 0$, it need be calculated only for positive x. The boundary conditions at $x = 0$ are $s = 0$, $h = H/2$ and $\kappa = 0$. Equations (2.7*b*)–(2.9) were solved using the modified Euler method. A non-uniform grid was used with very fine spacing near h equal to 0. h was solved for by starting at $x = 0$ with a given macroscopic interface angle. Integration was stopped at $h = 0$ and the found microscopic contact angle recorded as a function of the macroscopic angle and the other parameters.

The quasi-parallel equations are straightforward and rapid to solve. There were no difficulties in obtaining results down to and below $\epsilon_s = 10^{-7} H$.

2.2. *Fourier series method*

This solves the full Stokes equations using a Fourier series approach. It is valid provided $h(y)$ is single valued and provided the two fluids are equiviscous. Given that, it is applicable to all three flow geometries. The flow is taken to be periodic with period L, with L large enough so that interactions between menisci are negligible. With equiviscous fluids the Stokes equations can be written for the whole domain as

$$\mu\left(\frac{\partial^2 u}{\partial x^2} + \frac{\partial^2 u}{\partial y^2}\right) = \frac{\partial p}{\partial x} - \sigma\kappa_x(y,t)\delta(x - h(y,t)) - \tfrac{1}{2}g\rho_\delta K(x - h(y,t)), \tag{2.12a}$$

$$\mu\left(\frac{\partial^2 v}{\partial x^2} + \frac{\partial^2 u}{\partial y^2}\right) = \frac{\partial p}{\partial y} - \sigma\kappa_y(y,t)\delta(x - h(y,t)), \tag{2.12b}$$

$$\frac{\partial u}{\partial x} + \frac{\partial v}{\partial y} = 0. \tag{2.12c}$$

$K(\zeta)$ is a variant of the Heaviside function, equalling ± 1 and taking the sign of ζ. The delta function multiplied by the interface curvature multiplied by the surface tension gives the interfacial forcing. $\sigma\kappa_x$ and $\sigma\kappa_y$ are the x and y components of the

forcing:

$$\kappa_x = \frac{\kappa}{\sqrt{1+h_y^2}}, \quad \kappa_y = -\frac{h_y \kappa}{\sqrt{1+h_y^2}}, \tag{2.13}$$

$h(y,t)$ obeys

$$\frac{\partial h}{\partial t} = u - v h_y, \tag{2.14}$$

where the y subscript on h indicates the partial derivative. Note that the density has period $2L$. g reverses sign with period L in order to force the flow with the proper period and to keep the flow gravitationally stable.

The flow is divided into two parts, the parallel flow due to the moving plates and the periodic flow due to the interfacial forcing. The parallel flow is given by

$$U_p = U_{\mathrm{B}}^{\mathrm{F}} - \left(2U_{\mathrm{T}}^{\mathrm{F}} + 4U_{\mathrm{B}}^{\mathrm{F}}\right)(y/H) + \left(3U_{\mathrm{T}}^{\mathrm{F}} + 3U_{\mathrm{B}}^{\mathrm{F}}\right)(y/H)^2, \tag{2.15a}$$

where the top and bottom fluid speeds $U_{\mathrm{T}}^{\mathrm{F}}$ and $U_{\mathrm{B}}^{\mathrm{F}}$ are related to the wall speeds $U_{\mathrm{T}}^{\mathrm{W}}$ and $U_{\mathrm{B}}^{\mathrm{W}}$ through the equations

$$(4\lambda+1)U_{\mathrm{B}}^{\mathrm{F}} + (2\lambda)U_{\mathrm{T}}^{\mathrm{F}} = U_{\mathrm{B}}^{\mathrm{W}}, \quad (2\lambda)U_{\mathrm{B}}^{\mathrm{F}} + (4\lambda+1)U_{\mathrm{T}}^{\mathrm{F}} = U_{\mathrm{T}}^{\mathrm{W}}, \tag{2.15b}$$

where $\lambda = \epsilon_s/H$. The Fourier transform of a 'line' delta function is

$$\int_{-L/2}^{+L/2} \delta(x - h(y,t)) \mathrm{e}^{-\mathrm{i}\alpha m x} \mathrm{d}x = \sqrt{1+h_y^2}\, \mathrm{e}^{-\mathrm{i}\alpha m h(y)} \tag{2.16}$$

Multiplying equations (2.12a)–(2.12b) by $\mathrm{e}^{-\mathrm{i}\alpha m x}$ and integrating yields

$$\mu\left(\frac{\mathrm{d}^2 u_m}{\mathrm{d}y^2} - (\alpha m)^2 u_m\right) = \mathrm{i}\alpha m p_m - \frac{\sigma\kappa}{L}\mathrm{e}^{-\mathrm{i}\alpha m h} - \frac{\mathrm{i}g\rho_\delta}{\alpha m L}(\cos(\alpha m L/2) - \mathrm{e}^{-\mathrm{i}\alpha m h}), \tag{2.17a}$$

$$\mu\left(\frac{\mathrm{d}^2 v_m}{\mathrm{d}y^2} - (\alpha m)^2 v_m\right) = \frac{\mathrm{d}p_m}{\mathrm{d}y} + \frac{h_y \sigma\kappa}{L}\mathrm{e}^{-\mathrm{i}\alpha m h}. \tag{2.17b}$$

These can be combined with the transformed continuity equation to yield the stream-function equation

$$\mu\left(\frac{\mathrm{d}^4\psi_m}{\mathrm{d}y^4} - 2(\alpha m)^2\frac{\mathrm{d}^2\psi_m}{\mathrm{d}y^2} + (\alpha m)^4\psi_m\right) = \frac{1}{L}\left(\sigma\frac{\mathrm{d}\kappa}{\mathrm{d}y} - g\rho_\delta\frac{\mathrm{d}h}{\mathrm{d}y}\right)\mathrm{e}^{-\mathrm{i}\alpha m h}. \tag{2.18}$$

The boundary conditions are

$$\psi_m(0) = \psi_m(H) = 0, \quad \left.\frac{\mathrm{d}\psi_m}{\mathrm{d}y}\right|_0 = +\epsilon_s\left.\frac{\mathrm{d}^2\psi_m}{\mathrm{d}y^2}\right|_0, \quad \left.\frac{\mathrm{d}\psi_m}{\mathrm{d}y}\right|_H = -\epsilon_s\left.\frac{\mathrm{d}^2\psi_m}{\mathrm{d}y^2}\right|_H. \tag{2.19}$$

These equations were solved by discretizing on a non-uniform grid that had closer spacing near the walls. About 100–400 grid points were used and about 100–400 Fourier functions. The physical velocities were found at discrete $h_n(y_n,t)$ by summation and the interface shape advanced in time via (2.14).

Because of the non-uniform grid, there was no particular difficulty encountered in finding results down to $\epsilon_s = 10^{-4}H$. Calculations were time-accurate so some searching was required to find critical capillary numbers. The best way is to start above critical Ca and work down towards it. Just above criticality, interfaces have a near-equilibrium point through which they advance very slowly. Their minimum rate of advance is a linear function of $Ca - Ca_{cr}$ and the deviation of the macroscopic interface angle at which this minimum speed occurs from the critical macroscopic angle is also linear.

Thus, two supercritical calculations are sufficient to find both the critical capillary number and the critical macroscopic angle.

2.3. *Phase-field equations*

Two-and three-dimensional Stokes flow computations were made using a phase-field diffuse-interface method. Details of phase-field modelling and its applicability to moving contact lines are given in Seppecher (1996), Jacqmin (1999, 2000), and Pismen & Pomeau (2000). The phase-field interface model goes back to van der Waals (1893), who hypothesized finite-thickness fluid interfaces with excess free energy, or surface tension, proportional to the integral through the interface of $|\nabla C|^2$. $C(x, y)$, the phase function, represents the amount locally present of each fluid. The total free energy of the liquid mixture is taken to be of the form

$$F = \int \left(\tfrac{1}{2}\alpha(\nabla C)^2 + \beta f(C)\right) \mathrm{d}V. \tag{2.20}$$

$f(C)$ is a nonlinear function of C with two minima corresponding to the two stable phases. Away from interfaces, C tends to these two minimizing values. The interfaces have a structure determined asymptotically by the minimization of interfacial free energy.

The chemical potential corresponding to F is

$$\phi = \beta f'(C) - \alpha \nabla^2 C. \tag{2.21}$$

In interface regions, it is asymptotically equal to the local field curvature multiplied by the surface tension. For the calculations, two different forms of $f'(C)$ have been used, $f_1' = 4C(C^2 - 1/4)$ and $f_2' = -C + \gamma C/(1/4 - C^2)$. The second is a double-obstacle potential with singularities at $\pm 1/2$. This form is more difficult to use than the first, but it has advantages in that it gives sharper interfaces and allows less interphase solubility. Asymptotically, meaning as interface thickness goes to zero, the two formulations should give equivalent results. In the calculations, γ was assigned a value of 0.0032. This gives spinodal points ($f''(C) = 0$) at $C = \pm 0.46$.

The equations solved consist of the Stokes equations forced by the diffuse-interface surface tension

$$\mu\left(\frac{\partial^2 u}{\partial x^2} + \frac{\partial^2 u}{\partial y^2} + \frac{\partial^2 u}{\partial z^2}\right) = \frac{\partial p}{\partial x} - \phi\frac{\partial C}{\partial x} - \rho g, \tag{2.22a}$$

$$\mu\left(\frac{\partial^2 v}{\partial x^2} + \frac{\partial^2 v}{\partial y^2} + \frac{\partial^2 v}{\partial z^2}\right) = \frac{\partial p}{\partial y} - \phi\frac{\partial C}{\partial y}, \tag{2.22b}$$

$$\mu\left(\frac{\partial^2 w}{\partial x^2} + \frac{\partial^2 w}{\partial y^2} + \frac{\partial^2 w}{\partial z^2}\right) = \frac{\partial p}{\partial z} - \phi\frac{\partial C}{\partial z}, \tag{2.22c}$$

$$\frac{\partial u}{\partial x} + \frac{\partial v}{\partial y} + \frac{\partial w}{\partial z} = 0. \tag{2.22d}$$

plus the advective Cahn–Hilliard equation for the evolution of the phase function

$$\frac{DC}{Dt} = \nabla \cdot D(C)\nabla\phi. \tag{2.23}$$

$\phi\nabla C$ gives the interfacial capillary forcing. $D(C)$ is the mobility. When using f_1', D was set to a constant; for f_2', D was variable and in the vicinity of $\pm 1/2$ was set proportional to $1/f_2''$. The diffusive lengthscale relevant to contact line dynamics is $\sqrt{\mu D(0)}$ (Jacqmin 2000).

Equations (2.22–2.23) were solved in a long rectangle with aspect ratios of six or eight to one. The ends of the box were treated as no-stress boundaries. The moving sides were assigned the same Navier slip condition as used in the quasi-parallel analysis. This was large enough to dominate the effective slip given by the phase-field diffusion. Standard finite-difference methods were used for the velocities. The C field was discretized using a fourth-order-accurate mehrstellen method (Jacqmin 1999).

The same approach to finding the critical capillary numbers and macroscopic angles was used as for the Fourier series solutions. A problem with phase-field calculations is that interface energies are somewhat dependent on interface position within the computational grid. The result can be an unsmooth advance of the interface as it moves over what becomes effectively a 'rough' or 'dirty' solid wall. This dependence on grid position decays exponentially with the number of grid points through the interface (Jacqmin 1999). It can therefore be removed if the number of grid points in a computation is increased sufficiently, at the cost, however, of sometimes greatly increased computational times. Grid effects do not usually matter when qualitative results are required, for example, for three-dimensional tipstreaming, but they have occasionally caused problems when trying to make accurate comparisons to quasi-parallel and Fourier series results.

2.4. *Non-dimensional parameters*

Non-dimensional parameters for the quasi-parallel model are microscopic contact angle, macroscopic angle, capillary number $Ca = U_0\mu/\sigma$, where U_0 is a characteristic wall velocity, Bond number $B = \rho_\delta g H^2/\sigma$, and the microscopic to macroscopic length ratio $\lambda = \epsilon_s/H$. Of these five, four are independent. The two-dimensional Stokes-flow/phase-field model adds three more, box aspect ratio, the Cahn number ϵ_w/H, where ϵ_w is a measure of diffuse interface thickness, and a Péclet number based on interfacial thickness, $U_0\epsilon_w^2/D\sigma$. Calculations presented here have been made with Cahn numbers from 0.125 to 0.03125 and with Péclet numbers from 4 to 100. For the most part, results of interest have been found to be insensitive to variations in these parameters.

3. Non-uniqueness and criticality

For the most part, in the two-dimensional calculations we are interested in finding boundaries for the existence of steady-state solutions. These boundaries could be mapped in many ways, but the main concern is finding critical velocities or critical Ca. Another mapping of interest is critical macroscopic angle. These two parameters are functions of microscopic wetting angle, Bo, λ and flow geometry.

Results from the quasi-parallel equations are illuminating in these matters because they show the existence not only of stable steady states, but of unstable, and that the critical velocity or critical macroscopic angle mark the boundary between these two types of solution. Figure 2 shows a typical result for shear flow for macroscopic angle as a function of capillary number. For this $\theta_{mic} = 135°$, $\lambda = 10^{-5}$ and $Bo = 0$. A maximum capillary number exists beyond which there is no solution. For the case shown in figure 2, this critical Ca is 0.00359 and the corresponding critical macroscopic angle is 165°. Above the critical macroscopic angle, the solution branch moves back toward a lower capillary number. This upper branch of solutions is unstable and is unfindable via the time-stepping solution methods used for the Fourier-transform and phase-field calculations. Tabulation of the critical capillary number and macroscopic angle thus delineates the two-dimensional stability limits of these flows.

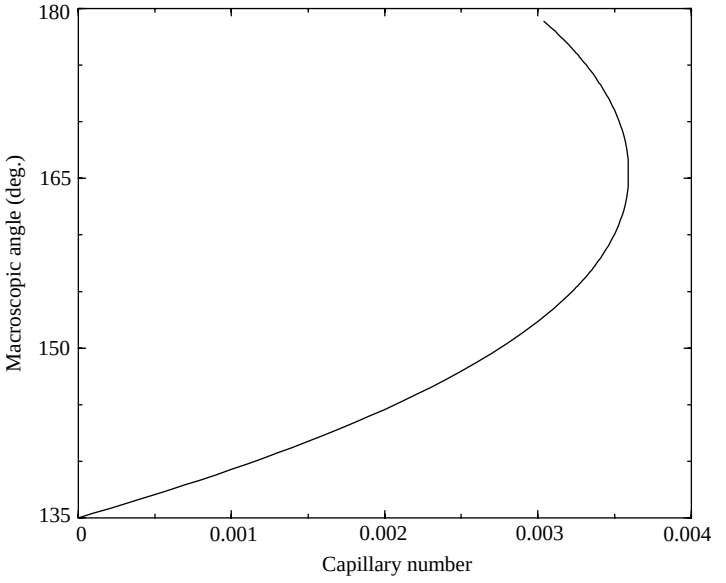

FIGURE 2. Macroscopic interface angle as a function of capillary number, for microscopic contact angle of 135°. $Bo = 0$, $\lambda = 10^{-5}$. Critical Ca about 0.00359, critical θ_{mac} about 165°. Data from quasi-parallel model.

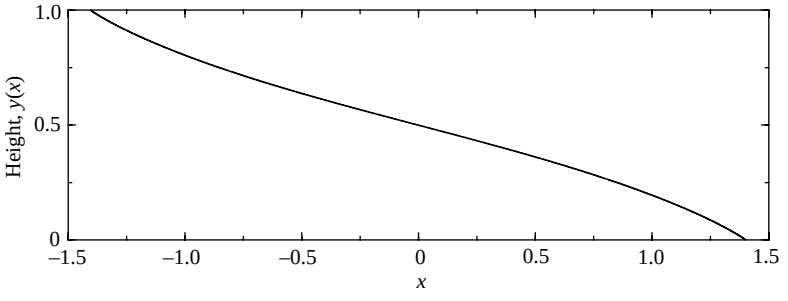

FIGURE 3. Critical interface corresponding to the critical point of figure 2. θ_{mac} about 165°, $\theta_{mic} = 135°$.

4. Shear flow

Figure 3 shows a typical shear flow critical interface shape, from which it can be seen that most of the interface away from the contact lines is close to its macroscopic centre-channel angle. This is the critical interface for the calculation discussed in the previous section. Of greatest interest is finding critical Ca and θ_{mac} as a function of flow parameters. Figure 4 shows quasi-parallel results for $\lambda = 10^{-7}, 10^{-5}, 0.001$ and 0.1. The critical capillary number decreases with decreasing λ while critical θ_{mac} increases. Both critical Ca and θ_{mac} show what appears to be an approximately logarithmic dependence on λ.

Critical θ_{mac} is relatively weakly dependent on θ_{mic}. Very roughly, at wetting angles away from 180°, instability sets in at about $\theta_{mac} = 150°$. Instability is caused by the increased global viscous forces that are brought to bear as θ_{mac} increases. The viscous-induced pressure in the two tongues of receding fluid increases with increasing θ_{mac}

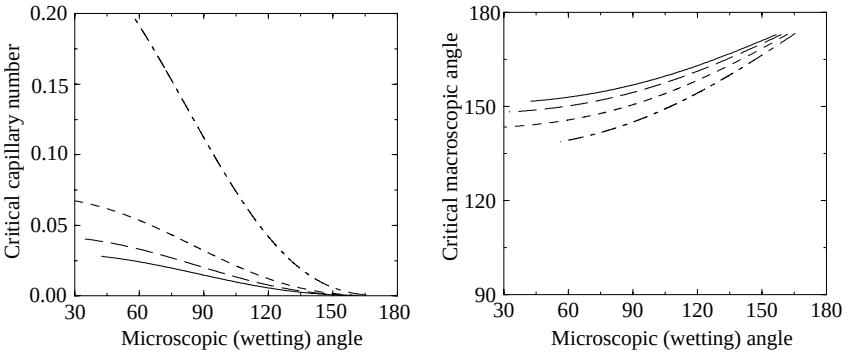

FIGURE 4. Critical capillary number and critical macroscopic angle as functions of microscopic contact angle, for $-\cdot-$, $\lambda = 0.1$; ---, 0.001; $-\,-\,-$, 10^{-5}; —, 10^{-7}, according to the quasi-parallel analysis.

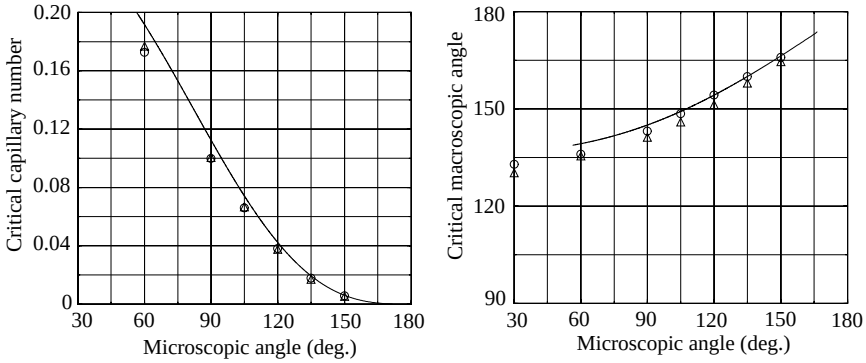

FIGURE 5. Critical capillary number and macroscopic angle as functions of microscopic contact angle for $\lambda = 0.1$. Bond number $= 0$. Quasi-parallel results are given by the solid line, Fourier series results by the circles, and phase-field results by the triangles.

until the interface can no longer be curved enough to resist it (the integral of the curvature is necessarily bounded).

Figures 5, 6 and 7 compare quasi-parallel, Fourier series and phase-field results for critical Ca and θ_{mac} for, respectively, $\lambda = 0.1$, 0.01 and 0.001. Phase-field results are shown only in the first two figures. Agreement is quite good.

Figure 8 shows the evolution of an unstable flow with $Ca = 0.0274$, $\theta_{mic} = 90^\circ$ and $\lambda = 0.001$. Critical Ca is 0.0273, so the flow is very slightly supercritical. The flow is calculated using the Fourier series method. For comparison, the figure also shows the critical interface (the dashed line) as calculated from the quasi-parallel model. The interface moves quickly to its near-equilibrium position, then advances very slowly until it passes it, then moves quickly again. Its speed of advance then asymptotes to a significant fraction of the plate speed. Its near-equilibrium position and the quasi-parallel critical interface are very close to each other.

5. Gravity effects

Gravity can significantly change critical Ca and θ_{mic}. This is true even at small λ, in the asymptotic regime where it is sometimes claimed that macroscopic effects can be ignored. Figure 9 shows quasi-parallel results for $\lambda = 10^{-7}$. At $Bo = 1$, Ca_{cr} is

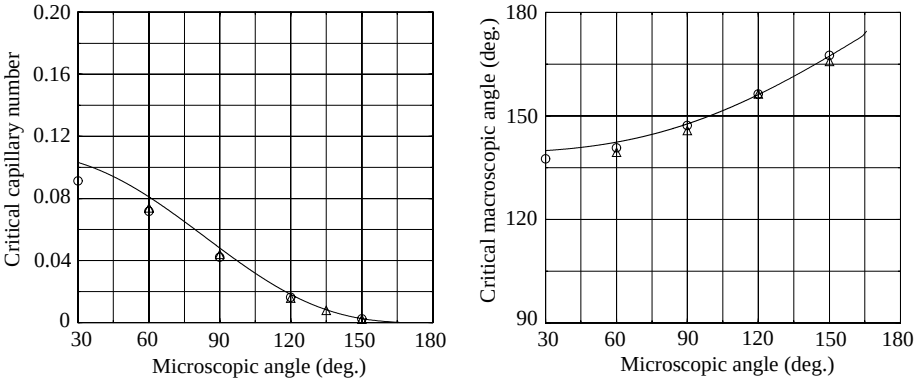

FIGURE 6. Critical capillary number and macroscopic angle as functions of microscopic contact angle for $\lambda = 0.01$. Bond number $= 0$. Quasi-parallel results are given by the solid line, Fourier series results by the circles, and phase-field results by the triangles.

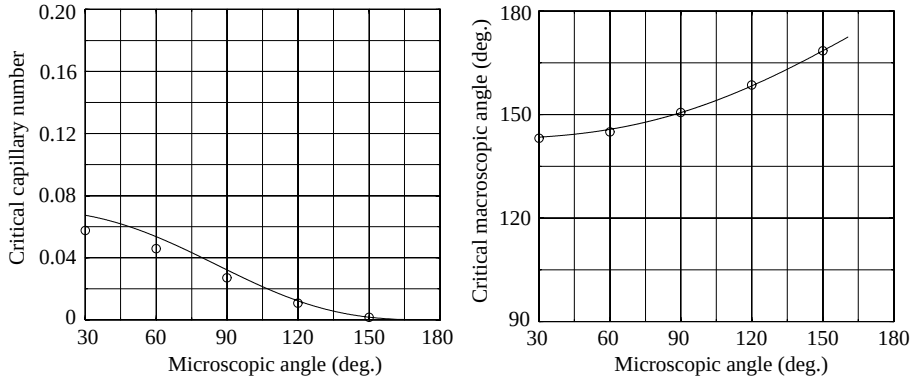

FIGURE 7. Critical capillary number and macroscopic angle as functions of microscopic contact angle for $\lambda = 0.001$. Bond number $= 0$. Quasi-parallel results are given by the solid line, Fourier series results by the circles.

increased by about 10% from $Bo = 0$; at $Bo = 4$, it is increased by about 25%. At high enough Ca_{cr} critical θ_{mac} is increased slightly from the zero-gravity case. As the wetting angle approaches 180°, however, stable wetting velocities become so small that gravity effects dominate over flow effects and the critical interface flattens. Thus, θ_{mac} diverges there from the zero-gravity case. With no gravity, as θ_{mic} goes to 180°, θ_{mac} also approaches 180°. For $Bo = 1$, the macroscopic angle instead asymptotes to a slope of about 141°, for $Bo = 4$, about 112°.

Figure 10 compares quasi-parallel Fourier series and phase-field critical Ca and θ_{mac} results for $Bo = 1$ for the case of $\lambda = 0.01$. Again, agreement among the three approaches is very good.

For higher Bond number, wetting failure is by film formation. This is shown in figure 11, which is similar to figure 8, but at a Bond number of 10. The critical quasi-parallel and Fourier series interfaces are shown together with an evolving supercritical interface at the start of film formation. Because of the gravity-induced flatness of parts of the interface, the quasi-parallel and Fourier series interfaces are no longer in quantitative agreement. Ca_{cr} is 0.0676 by the quasi-parallel analysis and about 0.0491

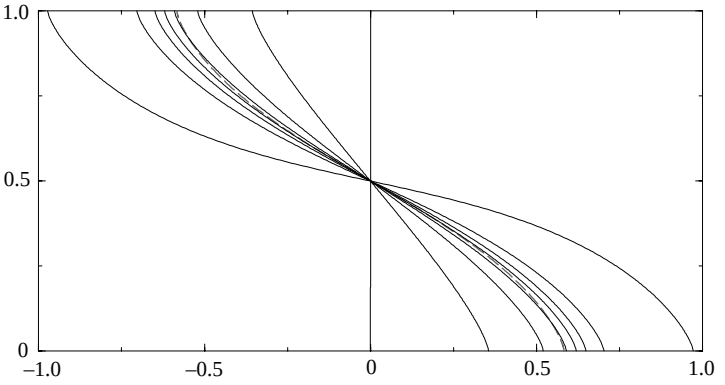

FIGURE 8. Evolution of an unstable interface calculated via the Fourier series method. Parameters are $Ca = 0.0274$, $Bo = 0$, $\lambda = 0.001$ and wetting angle $\theta_{mic} = 90°$. The flow is just past critical. The critical interface according to the quasi-parallel model is shown by the dashed line. The interface is initially flat. It is shown at non-dimensional times 0, 40, 200, 600, 1000, 1400, 1800 and 2200. (In this non-dimensionalization, the plate-speeds are equal to the capillary number.) The interface advances very slowly through its near-equilibrium position. The channel is infinitely long with interfaces spaced 8 units apart.

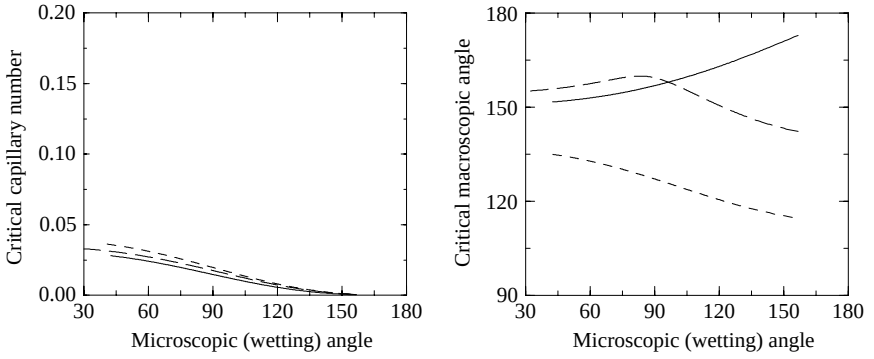

FIGURE 9. Critical capillary number and macroscopic angle as functions of microscopic contact angle for $\lambda = 10^{-7}$ and Bond numbers of 0 (solid curves), 1 (long-dashed curves) and 4 (dashed curves).

by the Fourier series method. The Fourier series simulation ends when the interface height $y = h(x)$ becomes multi-valued.

6. Driven capillary-rise flow and driven cavity flow

These flows were considered in order to see how changes in flow configurations or boundary conditions affect the onset of contact-line instability. They also provide a transition to the three-dimensional driven cavity flows considered next. The issue of how and whether contact line stability can be enhanced by flow geometry is a very practical one. For example, the maximum stable speed of wetting sets the processing rate for many industrial coating operations. Simpkins & Kuck (2003) and Blake, Bracke & Shikhmurzaev (1999) have discussed two industrially related coating methods that appear to increase wetting stability through the application of local pressure gradients.

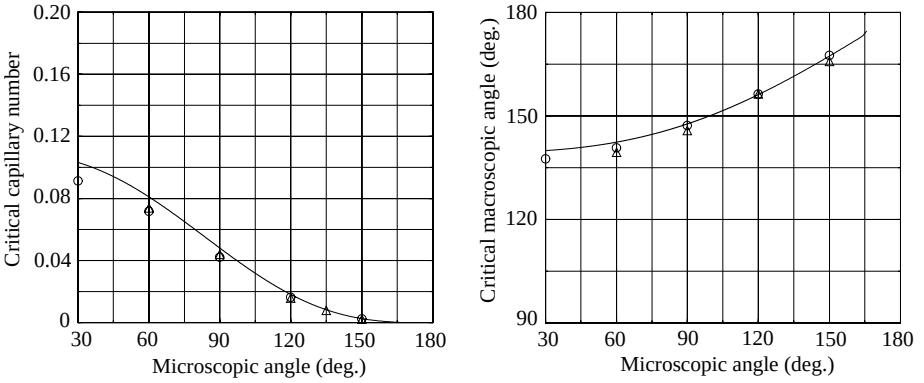

FIGURE 10. Critical capillary number and macroscopic angle as functions of microscopic contact angle for $\lambda = 0.01$. Bond number = 1. Quasi-parallel results are given by the solid line, Fourier series results by the circles, and phase-field results by the triangles.

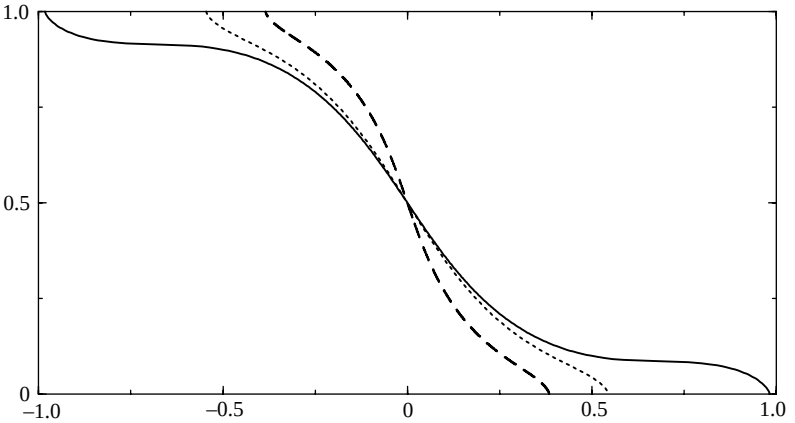

FIGURE 11. Film formation at $Bo = 10$, $\lambda = 0.001$, $\theta_{mic} = 90°$. The dashed line shows the quasi-parallel critical interface ($Ca = 0.0676$, $\theta_{mac} = 109.5°$), the dotted line the critical interface calculated using Fourier series ($Ca = 0.04914$, $\theta_{mac} = 122.57°$), and the solid line the unsteady supercritical interface ($Ca = 0.050$), also calculated using Fourier series, at an early stage of film formation.

As with the shear-flow case, we consider in this section only equiviscous flows. Figure 12 shows Fourier series and phase-field results for the stability limits for the two flows as a function of equilibrium wetting angle. λ is set to 0.01. As before, the agreement between the phase-field approach and the nearly exact Fourier series solution is quite good. The phase-field solution has a grid-point resolution of 96×768 and the diffuseness of the interface is such that the Cahn number is $1/24$.

Figure 13 compares the steady-state interface shapes and streamfunctions of the two solution methods for driven-capillary flow at $Ca = 0.12$ and an equilibrium wetting angle (of the lower flow) of 30°. Again, it can be seen that the two approaches are in good agreement. The details of the inner flow field, which changes considerably for sharp versus diffuse models, have little effect on the larger-scale flows and interface shapes.

Comparing stability limits among the flows (see figure 6 for the shear-flow case), we see a considerable variation of critical capillary number. The shear flow, for which the

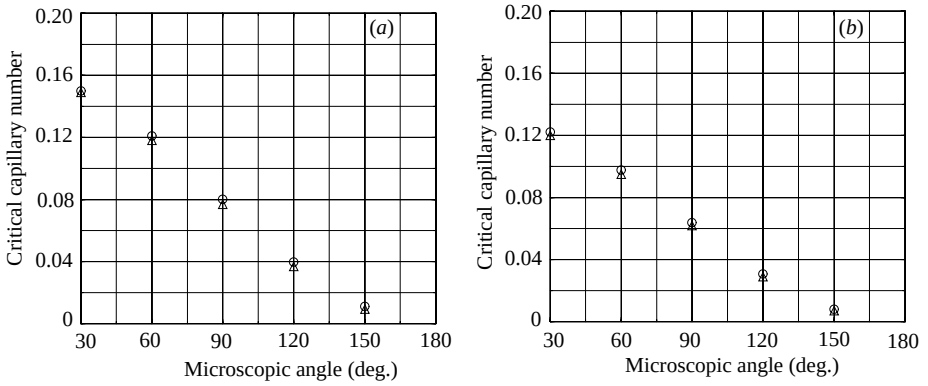

FIGURE 12. Critical capillary number as a function of microscopic contact angle for $\lambda = 0.01$. (*a*) Driven capillary flow; (*b*) driven cavity flow. Bond number = 0. Fourier results are given by the circles, phase-field results by the triangles.

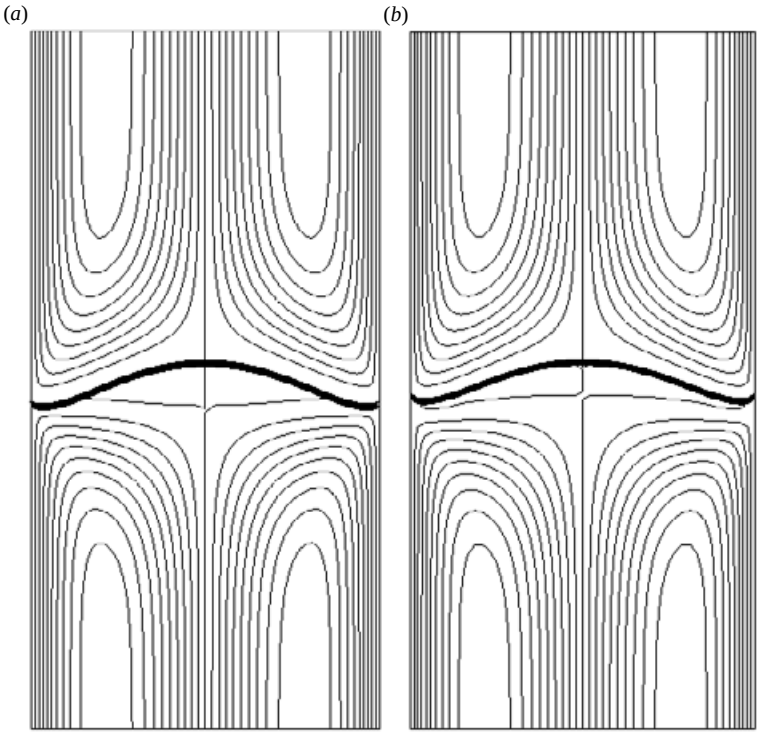

FIGURE 13. An example of interface shapes and flow fields as calculated using (*a*) the sharp-interface. Fourier series approach; (*b*) the phase-field method. The flow is driven-capillary at a $Ca = 0.12$ and with an equilibrium wetting angle of the lower fluid of 30°. Despite local differences at the wetting line, the two flows are globally in very good agreement.

oppositely moving walls tend most strongly of the three cases to stretch the interface, is the least stable. For the 90° equilibrium wetting angle, its critical capillary number is about 0.04, while for the driven cavity it is 0.06 and for the driven-capillary flow

0.08. At 30° the Ca_{cr} are, respectively, 0.09, 0.12 and 0.15. The driven-capillary case thus appears to be roughly twice as stable as the shear flow.

However, the question comes up as to whether or not this difference is due in part to the large value of λ and whether this difference becomes smaller as λ decreases (as the flow enters the asymptotic regime of $\lambda \to 0$). Calculations were therefore made with the Fourier series method for $\lambda = 0.001$. The results for the shear-flow case were given in figure 7. The shear-flow result for 90° is $Ca_{cr} = 0.0272$ while for the driven cavity and driven-capillary flows the critical Ca are, respectively, 0.0296 and 0.0333. The percentage difference between these two and the shear flow case declines so rapidly from the case $\lambda = 0.01$ that it appears it must go to zero as $\lambda \to 0$. We tentatively hypothesize that stabilization of wetting lines depends on physics outside that of the theory of incompressible and mutually insoluble fluids. A theory of high-speed wetting that incorporates solubility (of gas in liquid) has been proposed by Jacqmin (2002).

7. High-Bond-number three-dimensional tipstreaming as a quasi-two-dimensional process

It has usually (see discussion by Kistler 1993) been assumed that wetting fails only when the measurable macroscopic contact angle reaches 180°. By contrast, we have found that, in liquid–liquid flows, wetting failure occurs well before this. Associated with this, we have found that contact-line speed in an unstable two-dimensional flow is a non-monotonic function of macroscopic (or dynamic) angle – the minimum contact line speed is found at a quasi-equilibrium position; after passing that position the contact line speed increases.

Our phase-field calculations have found a high-Bond-number three-dimensional tipstreaming regime which seems to be at least partly understandable in these terms. They indicate that long-wave corrugations to an initially two-dimensional contact line can be unstable because the lowered parts of the interface have increased dynamic contact angle and associated with that an increased contact line speed. Contrariwise, the heightened parts have lower angle and therefore lowered speed. The corrugations thus increase in amplitude and, as the calculations have shown, eventually lead to tipstreaming.

From reports of others (Grace 1982) and our own three-dimensional calculations, for three-dimensional tipstreaming, the receding fluid must be considerably less viscous than the advancing. We consider here the case of a viscosity ratio of 0.1. There is no longer an advantage to considering oppositely moving walls (since no symmetry or antisymmetry is possible) so instead in these calculations only one wall is moving, the driven cavity case. Figure 14 shows the evolution of tipstreaming in three-dimensional two-phase flow in a box. In this view, all 6 walls are outlined. The front vertical wall is the moving wall. The wall opposite to it is motionless with no-stress conditions. The top and bottom walls are also no-stress. The rearward sidewall is no-slip while the frontward is actually a plane of symmetry. The no-slip sidewall introduces an asymmetry to the flow that seeds the tipstreaming. Amelioration of wetting and splitting singularities is provided by phase-field diffusion. The capillary number of the flow is 0.51, just above critical, the Bond number is 27.7, the Cahn number 0.059 and the Péclet number 2.63. λ (provided by the phase-field diffusion) is 0.025. The critical capillary number is higher than for the two-dimensional calculations because of the reduced viscosity of the receding fluid. The resolution of the computation was 48 side-to-side $\times$ 24 front-to-back $\times$ 96.

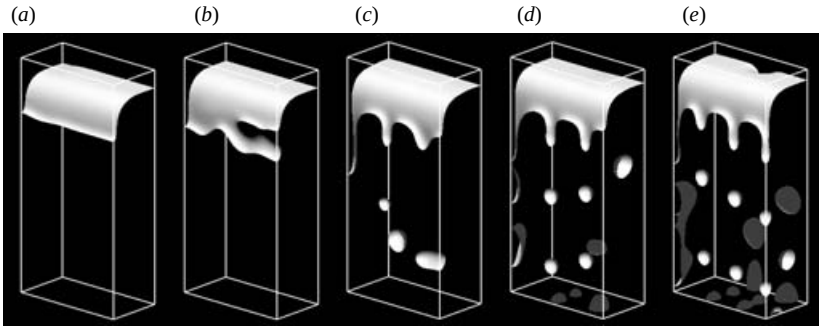

FIGURE 14. Three-dimensional film intrusion/tipstreaming. The front wall moves down, dragging a film of the upper lighter fluid. The frontward wall and rear sidewall are no-slip while the front side surface is a surface of symmetry. The initial breaking of the film (*b*) is primarily two-dimensional, but from this three-dimensional tip-streaming perturbations grow and develop (*c–e*). The film tips produce droplets at an approximately steady rate. The interface is shown with two shades, the dark shade means the advancing (lower) fluid side of the interface is facing the viewer, the light shade indicates the receding (upper) fluid. The droplets shown in light shade are attached to the front moving wall and are moving downward. The dark shaded droplets are attached to either the bottom surface or the rear wall, or are free-floating. After reaching the bottom of the container the droplets return because of buoyancy. The equilibrium contact angle for this calculation was set to 90°.

The flow is initially nearly two-dimensional (figure 14*a*). The no-slip rear sidewall introduces a perturbation because of drag that causes the contact line to move downward more slowly there. After a while, interface corrugations begin to spread from the rear sidewall region. These grow until the interface splits (figure 14*b*) in a quasi two-dimensional manner. After that, there is a quick transformation to tip streaming (figure 14*c*). Figures 14(*d*) and 14(*e*) show that the tipstreaming points can vary with time in number and length.

Another calculation, available on DVD from the author or the JFM Editorial Office, shows flow development when the rear sidewall, like the front, is made a plane of symmetry. Transition to tipstreaming is much delayed. As before, the flow is initially two-dimensional. As with the two-dimensional calculations (figures 8 and 11) the moving wall drags the interface down quickly at first, but then very slowly through its quasi-equilibrium position. Buoyancy-induced film instability then causes a cylindrical drop to detach and move down with the wall. When it reaches the bottom of the box it enters the bulk of the fluid and begins to rise. Rayleigh instability then takes over and the cylinder divides into droplets. As the droplets rise toward the surface they perturb the flow and contact-line corrugations begin to grow. The droplets reach the interface and the resulting large disturbance causes rapid wave growth at the contact line. This growth culminates in the tipstreaming instability which then continues in a quasi-periodic fashion.

Other calculations show that the range of capillary number that separates onset of instability from complete wetting failure (no or almost no wetting by the advancing fluid) is fairly narrow – about 0.04 for the viscosity ratio being considered. As the capillary number rises above critical, splitting instabilities (as shown in figure 14) become more important. There can be alternations between tipstreaming and splitting. As the capillary number is increased, tipstreaming alone is insufficient to prevent the interface from moving downward. The interface then elongates while also tipstreaming

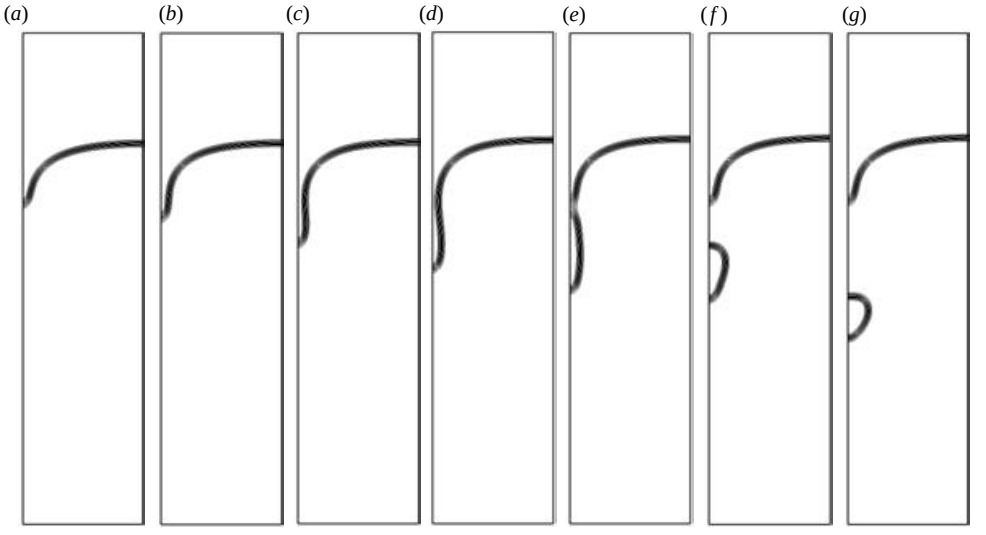

FIGURE 15. (*a*) The two-dimensional near-critical stable interface at $Ca = 0.375$, $Bo = 10$, viscosity ratio of 0.1. Side-view shown with moving wall on left, fixed wall on right. (*b–g*) One cycle of two-dimensional supercritical splitting, $Ca = 0.376$. Width of interface ($C = -0.4$ to $+0.4$) is shown. Time advances from left to right.

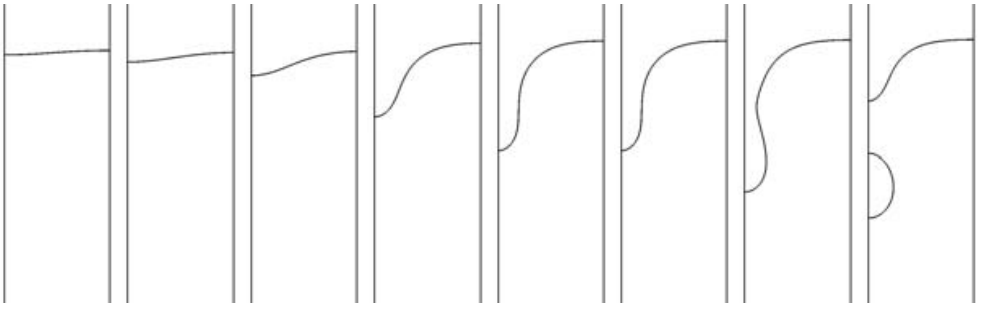

FIGURE 16. Initial growth of contact line corrugations leading to three-dimensional tip-streaming. Front view, showing the contact line on the moving wall. One-half wavelength of the contact line is shown – the line is symmetric about the left and right edges of the figures. Non-dimensional times shown are, from leftmost figure towards the right, 47, 57, 66, 72, 77, 80, 82 and 83. $C = 0$ is plotted. Ca is 0.38.

until a splitting event occurs that leaves the interface in a relatively high position again.

Some higher resolution ($12 \times 32 \times 128$) calculations have been made of periodically spaced tipstreaming. The calculation's wetting angle was 90°, the Bond number was 20, the viscosity ratio 0.1, the effective slip length, from Cahn–Hilliard diffusion, 0.02, the Cahn number 1/15, and the cell Péclet number 4. The two-dimensional Ca_{cr} was found to be just greater than 0.375 (about 0.3751) with a critical dynamic wetting angle (the maximum angle of the interface) of 161.6°. Figure 15(*a*) shows a side view of the two-dimensional near-critical interface at $Ca = 0.375$. Figures 15(*b*)–15(*g*) show the onset of instability through two-dimensonal splitting at $Ca = 0.376$. Three-dimensional calculations were made at $Ca = 0.38$. They were begun with a large-amplitude three-dimensional perturbation that led relatively quickly to tipstreaming. Figure 16 shows

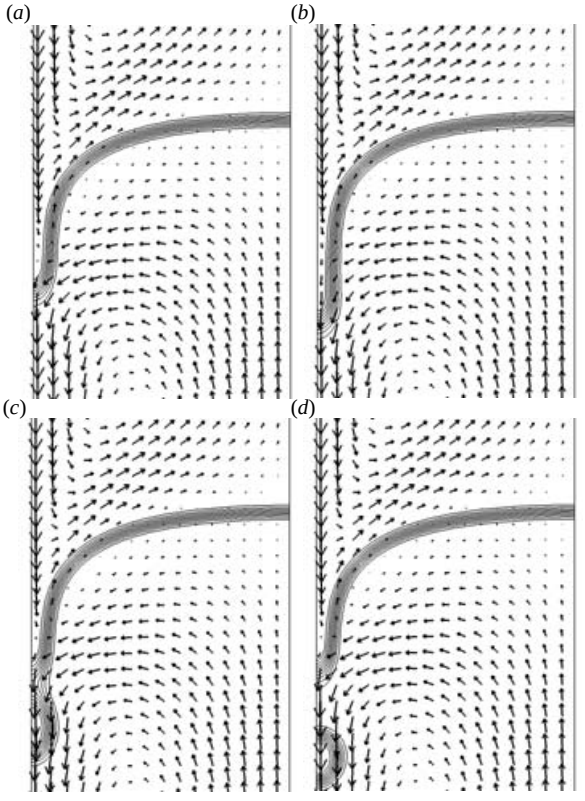

FIGURE 17. Drop pinch-off from tip, shown on the plane perpendicular to the tip. Interface and velocity field are shown at four times. Moving wall on left, fixed wall on right.

a front view of the evolution of the contact line. The figure shows half a wavelength of the line along the moving plate. Corrugations develop simultaneously with the lowering of the line as it is dragged down with the wall. They grow slowly at first but once the line moves to the quasi-equilibrium position they rapidly evolve to tipstreaming. Figure 17 shows a sideview of the interface together with the velocity field on a cut perpendicular to the tip. Four times are shown, in order to show drop pinch-off. From this view, it appears that the less viscous fluid channels or fingers into the more viscous. Note, however, that most of the less viscous fluid swept by the moving wall into the channel manages to return (escape). At time 1 (figure 17*a*) the flow in the finger is almost completely stopped. At time 2 (figure 17*b*) the interface has elongated so that viscous forces can no longer be balanced by capillarity and in the lower part of the finger the flow speed, forced by the moving wall, increases. The spatially non-monotonic flow in the finger causes an indentation (figure 17*c*) and then drop formation. The pinch-off, once initiated, is quite rapid. Figure 18 shows the flow field on a cut perpendicular to the contact line's crest. This is approximately steady. The maximum interface slope on this cut is about 158°, which is subcritical. The oscillation with time of this angle is less than a degree. Figure 19 shows the flow field in a cut parallel to the moving wall, half a computational cell distant. The moving contact line is shown plus the velocity close to the wall. It can be seen that the receding fluid is being diverted from the crest area into the tip. This maintains the crest's stability and comparative steadiness.

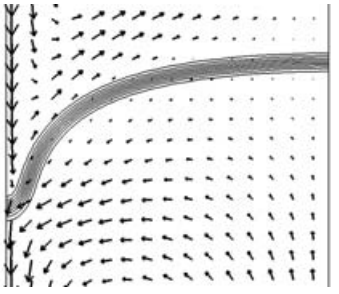

FIGURE 18. Quasi-steady interface and velocity field on the plane perpendicular to the contact line crest. Moving wall on left, fixed wall on right.

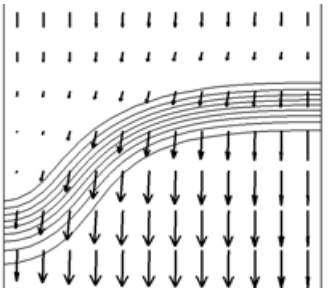

FIGURE 19. Diffuse-interface contact line and flow field near the moving wall. The upper, receding fluid is slightly diverted from the contact-line crest (on the figure's right-hand side) to the line's tip region.

An effort was made to find out if three-dimensional tipstreaming exists below the two-dimensional instability threshold. The capillary number of the calculation was therefore abruptly changed to 0.375, barely below critical. It was found that tipstreaming continued and was stable. When dropped to 0.374, however, tipstreaming quickly ceased and the flow reverted to being two-dimensional. The onset of tipstreaming thus appears to occur almost simultaneously with two-dimensional wetting failure.

8. Conclusions

This paper has attempted to show the feasibility and at least qualitative validity of calculations of wetting failure. Two-dimensional calculations have been made using three different methods and, in general, good agreement was shown amongst them. The phase-field method was then used to investigate three-dimensional wetting failure.

Results have shown:

(i) Qualitatively, two-dimensional results show little variation with λ once λ is below 0.01. This probably also holds true in three dimensions where small-λ calculations are not practical.

(ii) In liquid–liquid systems, wetting failure sets in well before the dynamic (macroscopic) angle reaches 180°.

(iii) Gravity significantly stabilizes flows against wetting failure.

(iv) From our $\lambda = 0.001$ calculations (end of § 6), change of flow boundary conditions or flow configurations may have little effect on flow stability. This tentative conclusion is limited to incompressible flow with insoluble fluids.

(v) In agreement with Grace (1982), tipstreaming during wetting occurs only when the receding fluid has much smaller viscosity than the advancing. When viscosities are the same, wetting failure is two-dimensional.

(vi) Three-dimensional wetting failure modes include both tipstreaming and splitting. The two modes can coexist.

(vii) Three-dimensional tipstreaming can be understood in part as a quasi-two-dimensional phenomenon. The three-dimensional critical capillary number is very close to the two-dimensional. In three-dimensional tipstreaming, tip regions appear to be locally two-dimensionally supercritical, while crests appear to be locally subcritical.

REFERENCES

Blake, T. D., Bracke, M. & Shikhmurzaev, Y. D. 1999 Experimental evidence of nonlocal hydrodynamic influence on the dynamic wetting angle. *Phys. Fluids* **11**, 1995–2007.

Blake, T. D. & Ruschak, K. J. 1979 Maximum speed of wetting. *Nature* **282**, 489–491.

Burley, R. & Jolly, R. P. S. 1984 Entrainment of air into liquids by a high-speed continuous solid-surface. *Chem. Engng Sci.* **39**, 1357–1372.

Eggers, J. 2001 Air entrainment through free surface cusps. *Phys. Rev. Lett.* **86**, 4290–4293.

Eggleton, C. D., Tsai, T. & Stebe, K. J. 2001 Tip streaming from a drop in the presence of surfactants. *Phys. Rev. Lett.* **87**, 048302.

Ghannum, M. T. &. Esmail, M. N. 1993 Experimental study of the wetting of fibers. *AIChE J.* **39**, 361–365.

Grace, H. P. 1982 Dispersion phenomena in high-viscosity immiscible fluid systems and the application of static mixers as dispersion devices in such systems. *Chem. Engng Commun.* **14**, 225–277.

Hocking, L. M. 1982 The spreading of a drop by capillary action. *J. Fluid Mech.* **121**, 425–442.

Huh, E. & Scriven, L. E. 1971 Hydrodynamic model of steady movement of a solid/liquid/fluid contact line. *J. Colloid Interface Sci.* **35**, 85–101.

Jacqmin, D. 1999 Calculation of two-phase Navier–Stokes flows using phase-field modeling. *J. Comput. Phys.* **155**, 96–127.

Jacqmin, D. 2000 Contact-line dynamics of a diffuse fluid interface. *J. Fluid Mech.* **402**, 57–88.

Jacqmin, D. 2002 Very, very fast wetting. *J. Fluid Mech.* **455**, 347–358.

Kistler, S. F. 1993 Hydrodynamics of wetting. In *Wettability* (ed. J. Berg), pp. 311–429. Marcel Dekker.

Pismen, L. M. & Pomeau, Y. 2000 Disjoining potential and spreading of thin liquid layers in the diffuse-interface model coupled to hydrodynamics. *Phys. Rev.* E **62**, 2480–2491.

Seppecher, P. 1996 Moving contact lines in the Cahn–Hilliard theory. *Intl J. Engng Sci.* **34**, 977–992.

Siegel, M. 2000 Cusp formation for time-evolving bubbles in two-dimensional Stokes flow. *J. Fluid Mech.* **412**, 227–257.

Simpkins, P. G. & Kuck, V. J. 2000 Air entrapment in coatings by way of a tip-streaming meniscus. *Nature* **403**, 641–643.

Simpkins, P. G. & Kuck, V. J. 2003 On air entrainment in coatings. *J. Colloid Interface Sci.* **263**, 562–571.

Somalinga, S. & Bose, A. 2000 Numerical investigation of boundary conditions for moving contact line problems. *Phys. Fluids* **12**, 499–510.

van der Waals, J. D. 1893 The thermodynamic theory of capillarity under the hypothesis of a continuous variation of density. *Verhandel/Konink. Akad. Weten.* **1**. English translation, *J. Statist. Phys.* **20**, 197–244.